Shahrood University of Technology

Journal of Hydraulic and Water Engineering (JHWE)

Journal homepage: https://jhwe.shahroodut.ac.ir

Iranian Hydraulic Association (IHA)

Three-Dimensional Numerical Modeling of Debris Flow for Hydrodynamic Analysis of Various Openings in Slit Check Dams

Seyed Nader Sadat Hosseini [*1], Ramin Amini [1], Amir Abass Abedini [1]

Department of Water and Environmental Engineering, Faculty of Civil Engineering, Shahrood University of Technology, Shahrood, Iran.

Article Info

Article history:

Received 22 July 2025
Received in revised form 30 November 2025
Accepted 14 December 2025
Published online 17 December 2025

DOI:10.22044/jhwe.2025.16556.1074

Keywords
Debris Flow
Slit Check Dam
Opening Sensitivity Analysis
CFD Modeling
Eulerian Multiphase
Flow Stability
Hydrodynamic Analysis

Abstract

Debris flows are among the most destructive natural phenomena in mountainous regions, and effective design of control structures for their management requires accurate analysis of the hydrodynamic behavior of the flow. In this study, using the OpenFOAM environment, debris flow is numerically simulated with the Eulerian–Eulerian multiphase model to investigate the effect of opening dimensions on the performance of slit check dams. Three different geometries with openings of 0.25, 0.5, and 0.75 times the flume width, along with a reference scenario without a check dam, were evaluated. The developed numerical model was validated against reliable experimental data and demonstrated appropriate accuracy in reproducing characteristics such as front arrival time, peak amplitude, and local flow fluctuations. The findings indicate that the opening width plays a decisive role in controlling the hydrodynamic behavior of the flow. The 0.5-flume-width opening offered the best balance between controlled passage, reduced fluctuations, and hydraulic flow stability, and is introduced as the optimal option. Although the 0.25-flume-width opening resulted in the greatest delay in peak detection at downstream sensors, it was accompanied by unstable behavior and severe fluctuations. Moreover, the 0.75-flume-width opening performed similarly to the no-dam scenario and showed limited effectiveness in restraining flow transfer. The results of this study can serve as engineering guidelines for the effective design of check dams to control debris flows in high-risk areas.

1. Introduction

Debris flow, composed of a mixture of rock or mud along with water, moves at high velocity. Rocks at the front of the debris flow are displaced downslope through rotational or sliding movement. These flows possess significant erosive power. The sediment concentration in debris flows is a criterion for their classification. If the flow contains a large proportion of coarse particles such as gravel, it is referred to as a *gravelly debris flow*. If the flow contains more fine particles relative to coarse particles like gravel, it is called a *muddy debris flow*. If the flow consists largely of cohesive fine-grained particles such as clay, it is termed a *cohesive debris flow* (Shrestha et al., 2008).

[*] *Corresponding author:* nadersadathosseini@shahroodut.ac.ir

Debris flow is defined as a type of high-concentration sediment flow in which at least 15 percent of the sediment weight includes coarse rock particles or carries woody debris. Sediment concentrations in such flows have been reported to reach up to 56 percent. Debris flows primarily occur in semi-arid, steep mountainous, and volcanic regions due to factors such as intense rainfall, rapid snowmelt triggered by volcanic lava, severe erodibility of volcanic ash, and movement of saturated soil masses following earthquakes (Tanhapour & Banihabib, 2019).

Key factors initiating debris flows typically include precipitation, sediment volume, and the slope of the flow bed. When rainfall is the primary cause, debris flows are initiated as landslides due to heavy precipitation. However, when sediment accumulation in the riverbed is the main factor, debris flow is triggered by bed erosion under the influence of flow-induced shear stress (Zhuang et al., 2015).

Debris flow is considered one of the most destructive and deadly natural hazards. It can lead to widespread human casualties, destruction of infrastructure, heavy economic losses, long-term environmental changes, and amplification of secondary hazards such as floods and subsequent landslides (Matthias Jakob, 2005).

In recent years, population growth and urban expansion have increased settlement in hazard-prone areas—regions that, despite their high agricultural and economic value, are highly vulnerable to phenomena such as debris flows. This alarming trend indicates that without proper risk management, the severity and extent of future natural disasters could far exceed past experiences (Voight, 1990).

Nevertheless, preventive measures can substantially reduce the damage caused by debris flows. Mitigation efforts typically fall into two categories: structural (hard) and non-structural (soft) measures. In leading countries such as Japan, the United States, South Korea, and many European nations, both types of measures are extensively and simultaneously employed for the management and reduction of debris flow impacts to achieve optimal outcomes (Huebl Johannes and Fiebiger, 2005; Vu, 2019).

(Huebl Johannesand Fiebiger, 2005; Vu, 2019).

Structural measures are designed to control, direct, and limit the movement of debris flows. These measures are employed to reduce destructive force and divert flows toward safer zones and include check dams, embankments, and guiding channels. To select optimal structural interventions, it is essential to thoroughly understand the behavior and mechanics of debris flows, since the characteristics of these flows vary depending on the geographical setting, flow types, and influencing factors (Mizuyama, 2008).

Non-structural measures refer to management, educational, legal, cultural, and communication strategies that enhance community resilience without physical construction. These include continuous monitoring, early warning systems, land-use planning and management, hazard mapping, public education, evacuation drills, multilayered information dissemination, institutional preparedness, and clearly defined responsibilities during crises (Chen & Wu, 2014).

Among the effective actions for controlling and directing debris flows to safe areas is the use of control structures such as check dams, which are considered practical and widely used structural solutions. Accurate design of these structures requires a sound understanding of the dynamic behavior of debris flow and its interaction with the structure. Generally, there are two main approaches for evaluating the performance of such structures: conducting physical experiments in laboratory settings and utilizing numerical methods.

In this study, numerical modeling is employed as a cost-effective and efficient method for analyzing the behavior of control structures against debris flow. In addition to significantly reducing design costs, numerical methods allow for the exploration of diverse scenarios and optimization of structural geometry without the need for constructing multiple physical models. Hence, this approach can enhance the accuracy of design and, by reducing time and expense, improve the performance and effectiveness of control structures in resisting debris flows.

In contrast to previous CFD-based debris flow studies that mainly applied two-phase (fluid–solid) formulations or simplified geometries, the present study adopts a three-phase Eulerian–Eulerian approach (air–slurry–solid) to better capture interfacial dynamics and entrained air effects. Additionally, the study provides quantitative engineering insights on the influence of slit opening ratios (0.25, 0.5, and 0.75 × flume width)—a configuration not previously examined in 3D multiphase OpenFOAM frameworks. This combination of physical validation, multiphase modeling, and parametric hydraulic assessment establishes the novelty and practical contribution of this work.

2. Materials and Methods

To conduct physical experiments related to debris flows, a laboratory flume—originally utilized in the referenced paper by (Baselt et al., 2021)—was employed. It was specifically designed to replicate real-world debris flow conditions at a laboratory scale. An overview of this flume is shown in Figure 1. The main components of the experimental system include:

(A) a general view of the flume with a smooth bed,

(B) an upstream reservoir equipped with a control gate,

(C) a top view of the release section with flow-deflecting walls,

(D) a flume with a rough surface,

(E) the location of ultrasonic and pressure sensors, and

(F) the downstream end of the flume and the flow-spreading plate.

The flume used in this study has a rectangular cross-section with a length of 12 meters, a width of 1.3 meters, and a depth of 0.3 meters, resulting in a cross-sectional area of 0.39 m². The bed slope is set at 19.1 degrees. At the end of the flume, a horizontal plate measuring 3.5 m × 3.67 m is installed to allow examination of sediment deposition and flow spreading after descending the slope.

At the upstream end, a prismatic reservoir is used to store a water-saturated mixture of particles, which is connected to the channel via a gate measuring 50 cm in width and 15 cm in height. This electronically controlled gate enables sudden and controlled release of the mixture. Additionally, deflector walls are installed on both sides of the reservoir outlet to prevent intense lateral impact of the flow during release.

In each test, 300 kilograms of a water-saturated mixture consisting of natural sand and gravel particles with nearly spherical shapes and a particle size distribution with d_{50} ranging from 1.34 to 5.84 millimeters was used. The physical properties of the mixture include a density of $\rho = 1000$ kg/m³ and a viscosity of $\mu \approx 0.001$ Pa·s. Once the gate is opened, the mixture flows rapidly down the flume under the influence of gravity and hydrostatic pressure. Although the inflow discharge is not directly reported, it can be estimated by dividing the total mass by the release duration. For example, if the release occurs over 10 seconds, the inflow discharge would be 30 kg/s.

To quantitatively measure flow parameters, the experimental system is equipped with various instruments, including ultrasonic sensors, load cells, and a digital camera operating at 50 frames per second. As shown in Figure 2, ultrasonic sensors (SonarBero 3RG Siemens) operating at a frequency of 50 Hz with an accuracy of ±0.5 mm were used to record the spatiotemporal variations in flow depth. The load cells used were model C9C 50N, embedded in a rubber-coated casing and installed within the channel bed to measure the vertical force exerted on the bed.

In total, eight measurement points were installed at four longitudinal sections located 1.75, 3, 4.25, and 5.5 meters from the reservoir outlet. At each section, one central sensor was positioned along the centerline of the flume (S1C to S4C), and lateral sensors (S3R, S3L, S2R, S2L) were placed 0.42 meters from the center. This arrangement enables a detailed examination of the lateral distribution and cross-sectional development of the debris flow (Baselt et al., 2021).

Due to the precise experimental design, high-quality recorded data, and the availability of key parameters required for reconstructing physical conditions, the experiments presented in the article *"Evolution of stony debris flows in laboratory experiments"* were selected as the primary reference for validating the numerical model used in this study. Furthermore, the compatibility of the flume geometry, mixture specifications, and flow release method with the numerical domain modeled in OpenFOAM enables a reliable comparison between numerical and experimental results. This selection provides a robust foundation for evaluating the model's performance in reproducing the dynamic behavior of debris flow.

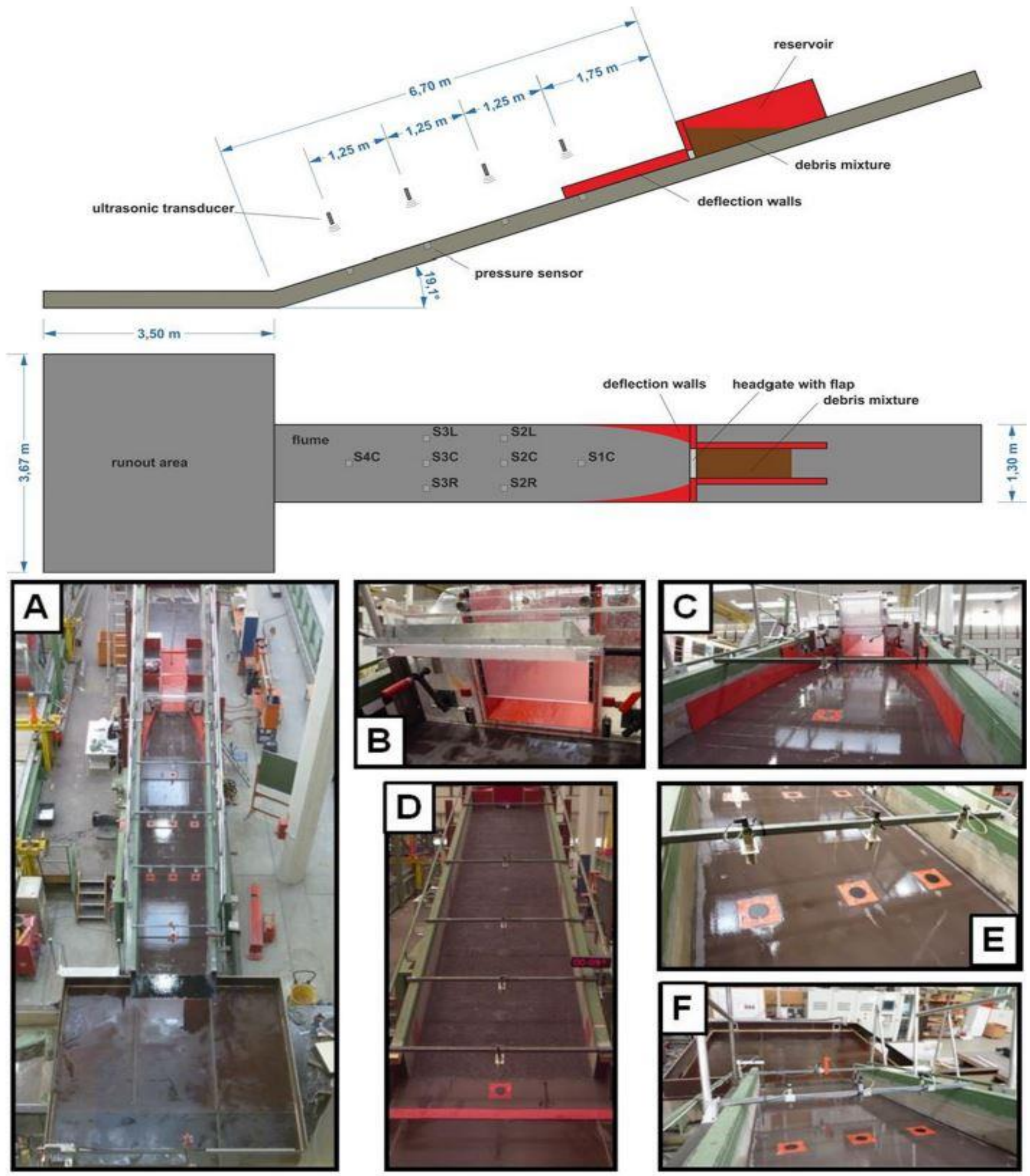

Figure 1. Dimensions and geometry of the laboratory flume and the initial location of the debris flow (Baselt et al., 2021)

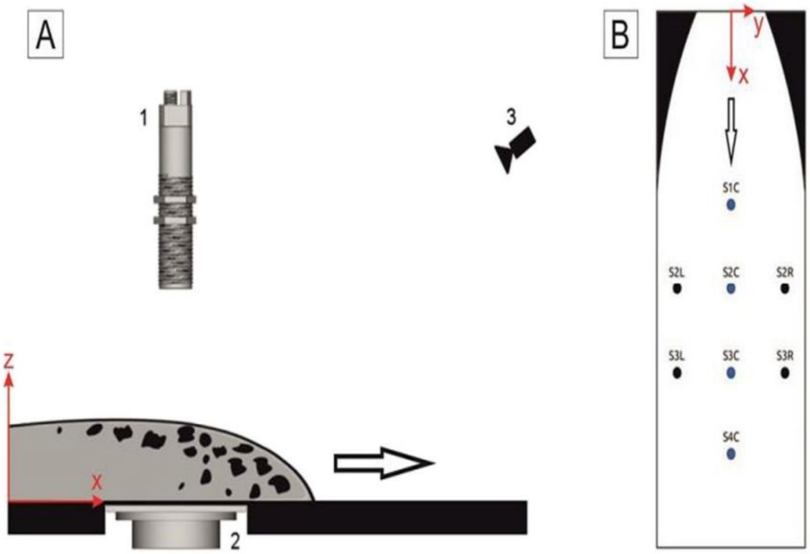

Figure 2. Panel A: Schematic side view of the measurement arrangement: 1. Ultrasonic sensor, 2. Pressure sensor, 3. Video camera; Panel B: Measurement locations (Baselt et al., 2021)

2.1. Experimental Flow Depth Data in the Laboratory Flume

To investigate the hydrodynamic behavior of debris flow, experimental data obtained from flow depth measurements along the central axis of the flume were utilized. These data were recorded using Siemens SonarBero 3RG ultrasonic sensors with a sampling rate of 50 Hz at four specific locations (S1C to S4C). The sensors were installed along the central axis of the flume at defined distances from the release reservoir.

Figure 3 presents the flow depth hydrograph at these locations as a function of time. As shown in the graph, the arrival of the flow front, the occurrence of the initial peak, and the gradual decline in flow depth are clearly observable. These experimental data were subsequently used as a reference for validating the numerical model (Baselt et al., 2021).

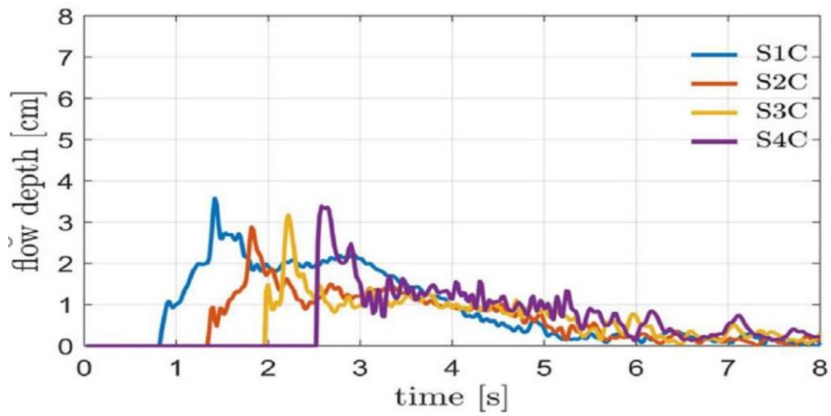

Figure 3. Variations in flow depth over time at four positions along the central axis of the flume (S1C to S4C) (Baselt et al., 2021)

2.2. Governing Equations and Multiphase Modeling

The three-phase model used in this study consists of air, slurry, and solid particles (gravel). This model, derived from the multi-fluid approach, has been investigated in various studies (Bohorquez, 2012; Damián & Nigro, 2014; Li et al., 2019).

2.3. Continuity Equations

For each phase, the continuity equations are defined as follows:

$$\frac{\partial \alpha_a \rho_a}{\partial t} + \nabla (\alpha_a \rho_a U_a) = 0$$
$$\frac{\partial \alpha_g \rho_g}{\partial t} + \nabla (\alpha_g \rho_g U_g) = 0 \quad (1)$$
$$\frac{\partial \alpha_s \rho_s}{\partial t} + \nabla (\alpha_s \rho_s U_s) = 0$$

where α_a, α_g, and α_s are the volume fractions of air, gravel, and slurry, respectively, satisfying the relation $\alpha_a + \alpha_g + \alpha_s = 1$. ρa, ρg, and ρs denote the densities of air, gravel, and slurry, respectively. U_a , U_g , and U_s represent the velocities of air, gravel, and slurry, respectively. By summing these three equations and dividing by density, the volumetric continuity equation is obtained as follows:

$$\nabla U = 0 \quad (2)$$

where $u = \alpha_a U_a + \alpha_g U_g + \alpha_s U_s$ represents the volumetric flow rate.

2.4. Momentum Equations

The momentum equations for each phase are expressed as follows:

$$\frac{\partial \alpha_a \rho_a U_a}{\partial t} + \nabla (\alpha_a \rho_a U_a U_a) - \nabla (\alpha_a \tau_a) = \alpha_a \rho_a g - \nabla P_a$$
$$\frac{\partial \alpha_g \rho_g U_g}{\partial t} + \nabla (\alpha_g \rho_g U_g U_g) - \nabla (\alpha_g \tau_g) = \alpha_g \rho_g g - \alpha_g \nabla P_g - F \quad (3)$$
$$\frac{\partial \alpha_s \rho_s U_s}{\partial t} + \nabla (\alpha_s \rho_s U_s U_s) - \nabla (\alpha_s \tau_s) = \alpha_s \rho_s g - \alpha_s \nabla P_s + F$$

where P_a, P_g, and P_s are the pressures of the air, gravel, and slurry phases, respectively, and τ_a, τ_g, and τ_s are the shear stresses of the three phases. g is the gravitational acceleration, and F represents the interaction force between the slurry and gravel. By combining the momentum equations of the three phases, the overall momentum equation for the mixture is obtained as follows:

$$\frac{\partial \rho U}{\partial t} + \nabla (\rho U U) - \nabla (\tau + \tau_m) = -\nabla P + \rho g \quad (4)$$

where

$$U = \frac{1}{\rho} (\alpha_a \rho_a U_a + \alpha_g \rho_g U_g + \alpha_s \rho_s U_s) = u + \alpha_g (1 - \alpha_g) \frac{\rho_g - \rho_s}{\rho} U_{gs} \quad (5)$$

where U_{gs} is the relative velocity of gravel with respect to the slurry, which can be expressed as (Damián & Nigro, 2014)

$$U_{gs} = U_r (1 - \alpha_g)^a \quad (6)$$

where U_r and a are constants. U_r can be considered as the average settling velocity of solid particles in a stationary liquid:

$$U_r = \frac{d^2}{18 \mu_s} (1 - \alpha_g)^5 (\rho_g - \rho_s) g \quad (7)$$

where d is the particle diameter and μ_s is the viscosity of the slurry.
The pressure of the mixture, \(P \), is defined as:

$$P = P_a + P_g + P_s \quad (8)$$

The volumetric stress tensor, τ, is given by:

$$\tau = \alpha_a \tau_a + \alpha_g \tau_g + \alpha_s \tau_s \quad (9)$$

The interaction stress tensor, τ, representing the stress arising from the relative motion of gravel with respect to slurry, is defined as:τ

$$\tau_m = -\alpha_g (1-\alpha_s) \frac{\rho_s \rho_g}{\rho_m} U_{gs} U_{gs} \quad (10)$$

where $\rho_m = \alpha_g \rho_g + \alpha_s \rho_s$ is the density of the gravel–slurry mixture.

2.5. Pressure and Hydrostatic Correction

To prevent numerical errors caused by hydrostatic pressure, the pressure is decomposed as follows (Berberović et al., 2009):

$$P = P_{rgh} + \rho g h \quad (11)$$

and its gradient is incorporated into the momentum equations as:

$$\nabla P = \nabla P_{rgh} + gh \nabla \rho + \rho g \quad (12)$$

where is the dynamic pressure, and isis the position vector.P_{rgh} h

By substituting Equation (12) into the momentum equation (Equation 4), we obtain the following relation (considering surface tension):

$$\frac{\partial \rho U}{\partial t} + \nabla(\rho U U) - \nabla(\tau + \tau_m) = -\nabla P_{rgh} - gh \nabla \rho + \sigma_k \nabla \alpha \quad (13)$$

The viscous stress tensor term in Equation (13) can be expressed as:

$$\nabla \ \tau = \nabla \left(\mu (\nabla U + \nabla U^T)\right) = \nabla (\mu \nabla U) + \nabla U \ \nabla \mu \quad (14)$$

where T denotes transpose. By substituting Equation (14) into Equation (13), the following expression is obtained:

$$\frac{\partial \rho U}{\partial t} + \nabla(\rho U U) - \nabla(\mu \nabla U) - \nabla U \nabla \mu - \nabla \tau_m = -\nabla P_{rgh} - gh \nabla \rho + \sigma_k \nabla \alpha \quad (15)$$

Dividing the air-phase continuity equation (Equation 1) by ρ_a, we obtain:

$$\frac{\partial \alpha_a}{\partial t} + \nabla(\alpha_a U_a) = 0 \quad (16)$$

Since air is immiscible with the slurry–gravel mixture, α_a defines the interface between air and the mixture. The volumetric velocity can be expressed as:

$$u = \alpha_a U_a + (1-\alpha_a) u_m \quad (17)$$

where $u_m = \alpha_g U_g + \alpha_s U_s$ is the volumetric velocity of the slurry–gravel mixture. Only the interaction between slurry and gravel is considered; hence, it is assumed that $u_m = u_a$. Therefore, Equation (16) can be rewritten as:

$$\frac{\partial \alpha_a}{\partial t} + \nabla(\alpha_a u) = 0 \quad (18)$$

2.6. VoF Model for the Air Phase

To track the air–mixture interface, the Volume of Fluid (VoF) method was employed (Albadawi et al., 2013):

$$\frac{\partial \alpha_a}{\partial t} + \nabla(\alpha_a u) + \nabla\left(\alpha_a (1-\alpha_a) c |u| \frac{\nabla \alpha_a}{|\nabla \alpha_a|}\right) = 0 \quad (19)$$

where c is the compression coefficient.

2.7. Phase Fraction and Solid Slip Equations

The velocity of gravel, U_g, can be expressed as:

$$U_g = u + (1-\alpha_s) U_{gs} \quad (20)$$

Finally, the volume fraction equation for the solid phase, incorporating a diffusion term, is given by:

$$\frac{\partial \alpha_g}{\partial t} + \nabla\left(\alpha_g u\right) + \nabla\left(\alpha_g (1-\alpha_g) U_{gs}\right) - D_{gs}\nabla^2 \alpha_g = 0 \quad (21)$$

where D_{gs} is the diffusion coefficient between the slurry and gravel phases, assumed to be negligible (value set as 1×10−61 (1×10^{-6})).

By solving Equations (16) and (21), the phase fractions of air and gravel can be obtained. The slurry phase fraction is the determined based on (Zhang et al., 2022):

$$\alpha_s = 1 - \alpha_a - \alpha_g \quad (22)$$

2.8. Geometry and Numerical Mesh

To numerically simulate debris flow and validate the developed model, the physical geometry of the experimental flume was reconstructed based on the study "Evolution of stony debris flows in laboratory experiments." This geometry includes a sloped flume, a rectangular inlet section, and an initial reservoir for the release of the flow, designed to replicate the sudden injection of debris flow. Figures 4 through 6 present the 3D views of the numerical geometry, which was designed and meshed using the software Pointwise.

In designing the geometry, every effort was made to accurately reproduce all physical details of the original experimental setup, including the flume dimensions, reservoir length and width, bed slope, and sensor locations. The coordinate system was defined in a standard manner, with the X-axis aligned with the flow direction, the Y-axis vertical, and the Z-axis across the flume width.

The computational domain was meshed using Pointwise, a specialized tool widely recognized for generating high-quality computational grids for CFD problems. The total number of computational cells in the domain is approximately 1.2 million.

The quality of the generated mesh was carefully evaluated based on metrics such as skewness, orthogonality, and aspect ratio, and found to be within acceptable limits for the solvers used in OpenFOAM. Utilizing a high-quality mesh plays a critical role in reducing numerical oscillations, improving solution stability, and enhancing the accuracy of predictions related to the time evolution of the free surface and the distribution of solid phases.

The boundary conditions were defined to realistically reproduce the hydraulic behavior observed in the laboratory flume. At the upstream boundary, a constant velocity corresponding to the experimental discharge was imposed, allowing the inflow hydrograph to enter the computational domain smoothly. The downstream boundary was treated as a free outflow section where both velocity and pressure were adjusted to prevent artificial reflections. Along the side walls and the channel bed, a no-slip condition was applied to represent viscous shear and wall friction effects, while the top boundary was modeled as an open free surface through which pressure variations could dissipate naturally. Considering the short duration of the debris surge and the relatively high mixture viscosity ($Re \approx 10^3$–10^4), the flow regime was assumed to be laminar. These boundary treatments effectively replicate the experimental flow conditions and ensure hydraulic and numerical stability throughout the computational domain.

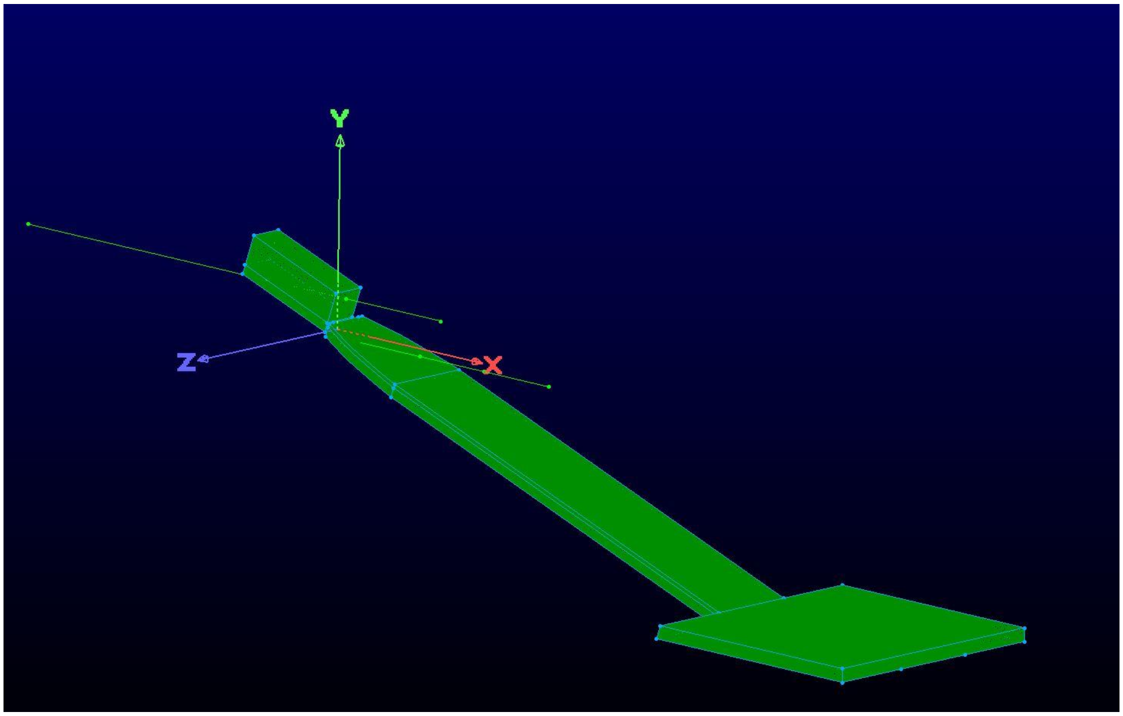

Figure 4. 3D view and mesh generation of the laboratory flume using Pointwise software

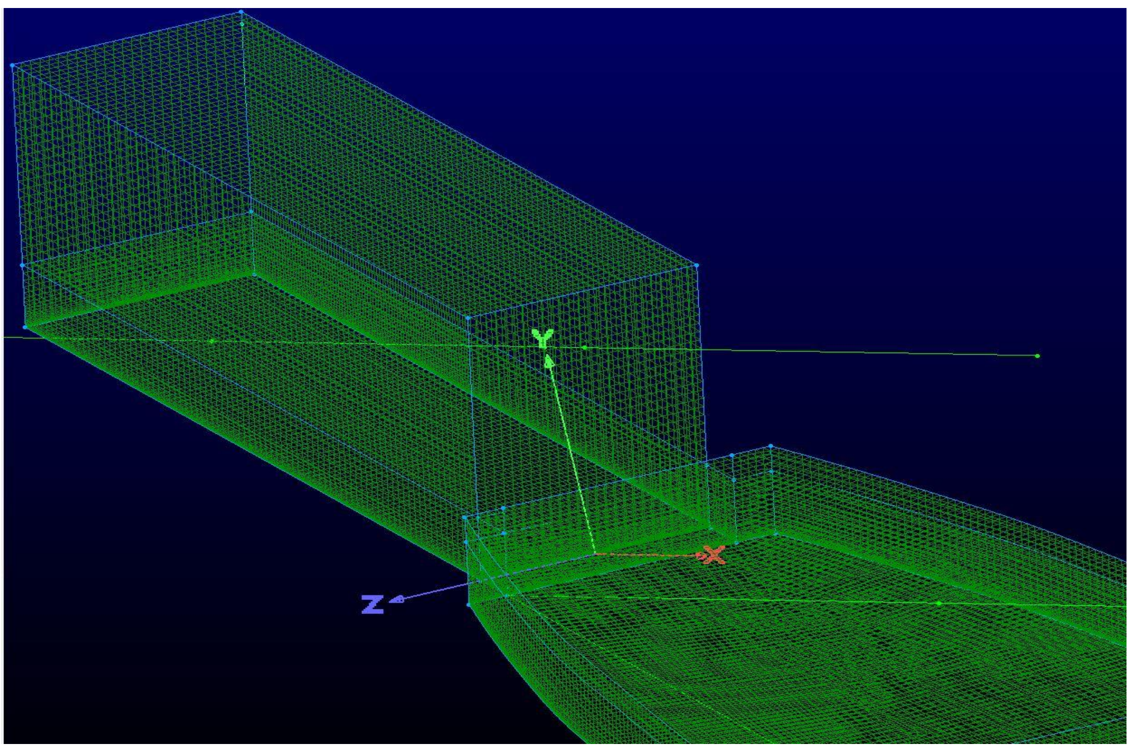

Figure 5. Mesh generation at the inlet section and around the reservoir using Pointwise software

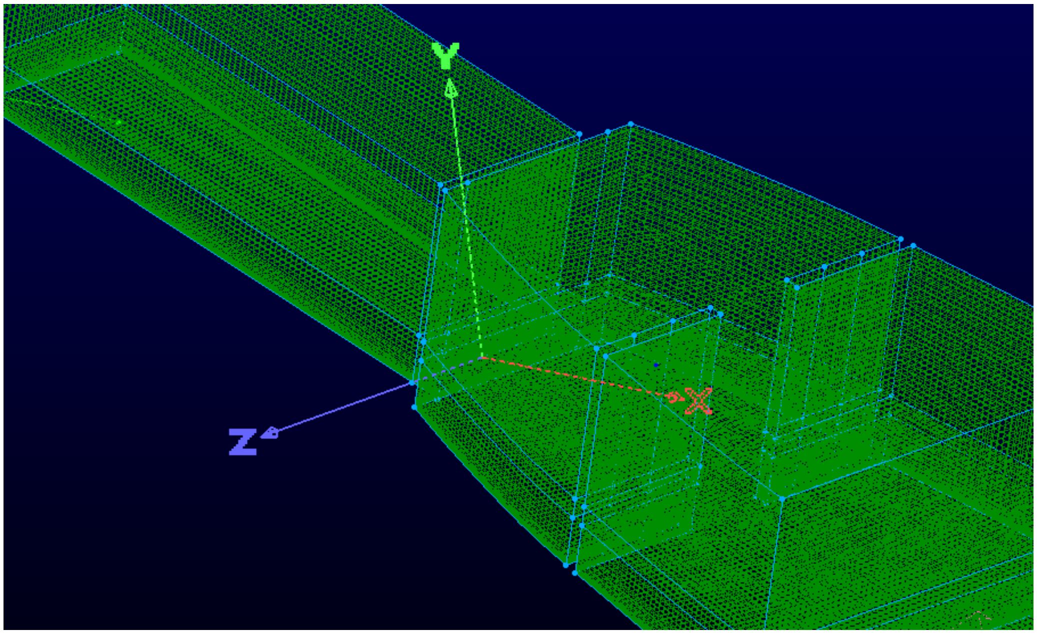

Figure 6. Mesh generation of the check dam using Pointwise software

3. Results and Discussion

3.1. Validation of the Numerical Model Using Experimental Data

As previously noted, to evaluate the accuracy and capability of the developed numerical model in reproducing the real behavior of debris flows, the results from a published experimental study titled "Evolution of stony debris flows in laboratory experiments" were used as the primary validation reference. In that study, the evolution of flow depth along a laboratory flume was measured using ultrasonic sensors at four different locations along the flume's central axis.

The experimental conditions included a smooth surface, fine particles, and a solid phase volume fraction of $\alpha s=0.47$. These physical conditions were accurately replicated in the numerical model.

In this study, the debris flow was simulated using an Eulerian–Eulerian multiphase approach within the OpenFOAM environment. In this framework, each of the solid and liquid phases is modeled as a continuous medium, with the governing equations of mass and momentum conservation solved independently for each phase. This approach, while accounting for interphase interactions, provides a robust capability to represent complex flows such as debris flows.

For model validation, flow depth values at positions corresponding to the ultrasonic sensors were extracted from the simulation using point-probe outputs. These outputs consist of time-series data for flow depth at four distinct positions along the channel. The resulting comparison between numerical and experimental data is shown in Figure 7.

In this graph, the experimental data are presented as colored data points, while the numerical simulation results are shown as continuous curves. To distinguish the sensors, blue, orange, and yellow colors represent Sensors 1, 2, and 3, respectively.

The comparison between numerical and experimental results indicates that the numerical model successfully reproduces the general trend of flow evolution. In particular, the model demonstrates good performance in capturing the arrival time of the flow front, the initial surge peak, and the gradual decay of flow depth during the post-front propagation phase. Moreover, the numerical model can simulate the local fluctuations in flow depth observed in the experimental data with a satisfactory level of accuracy. Given the relatively good agreement between the simulation results and the experimental observations, it can be concluded that the developed numerical model possesses sufficient scientific validity for analyzing debris flows under similar laboratory conditions. This validation provides a solid foundation for applying the model to more complex and advanced scenarios in the continuation of the research.

A grid-sensitivity analysis was conducted using three different meshes containing 0.9 × 10^6, 1.2 × 10^6, and 1.6 × 10^6 cells. The maximum variation in peak flow depth at Sensor S2 was less than 1.8%, confirming grid independence and numerical stability. Consequently, the selected mesh (~1.2 million cells) was adopted for all subsequent simulations as it provides sufficient resolution without unnecessary computational cost.

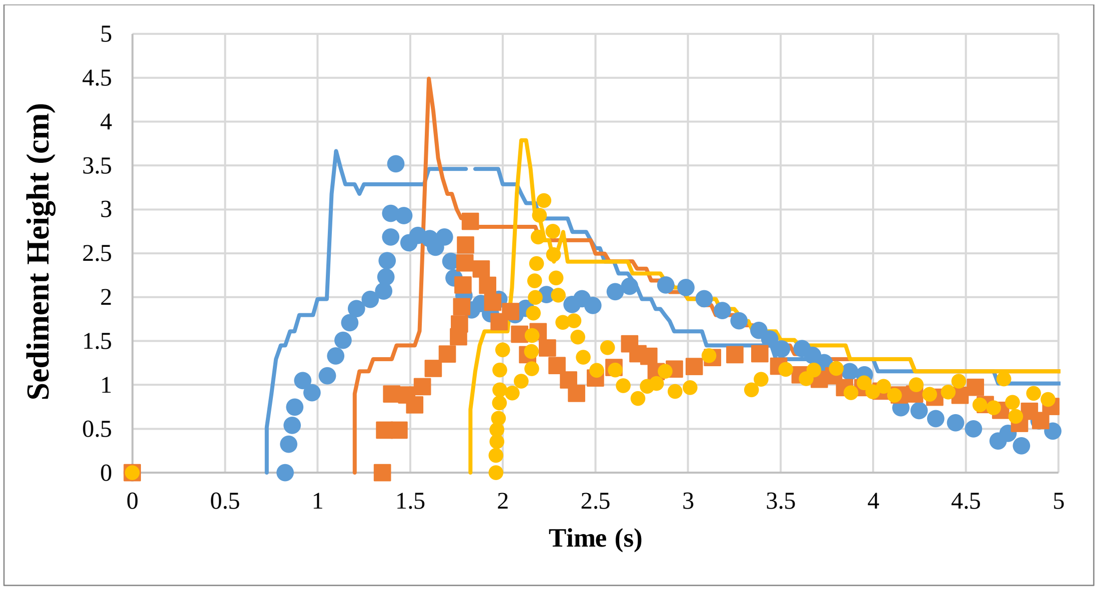

Figure 7. Comparison of experimental results and numerical model predictions

3.2. Investigation of the Effect of Check Dam Geometry with Different Openings on Debris Flow

In this section, to analyze the hydrodynamic performance of slotted check dams with various openings under debris flow conditions, four numerical scenarios were designed and examined. These include a case without any check dam (i.e., no obstruction in the flow path) and check dams with openings equal to 0.75, 0.5, and 0.25 times the flume width. The computational domain has physical dimensions similar to those of the laboratory flume.

As shown in Figure 8, the check dam is located 0.87 meters downstream from the inlet, positioned upstream of the first data recording sensor. This placement allows for detailed analysis of the influence of the structure's presence and geometry on flow characteristics along the flume.

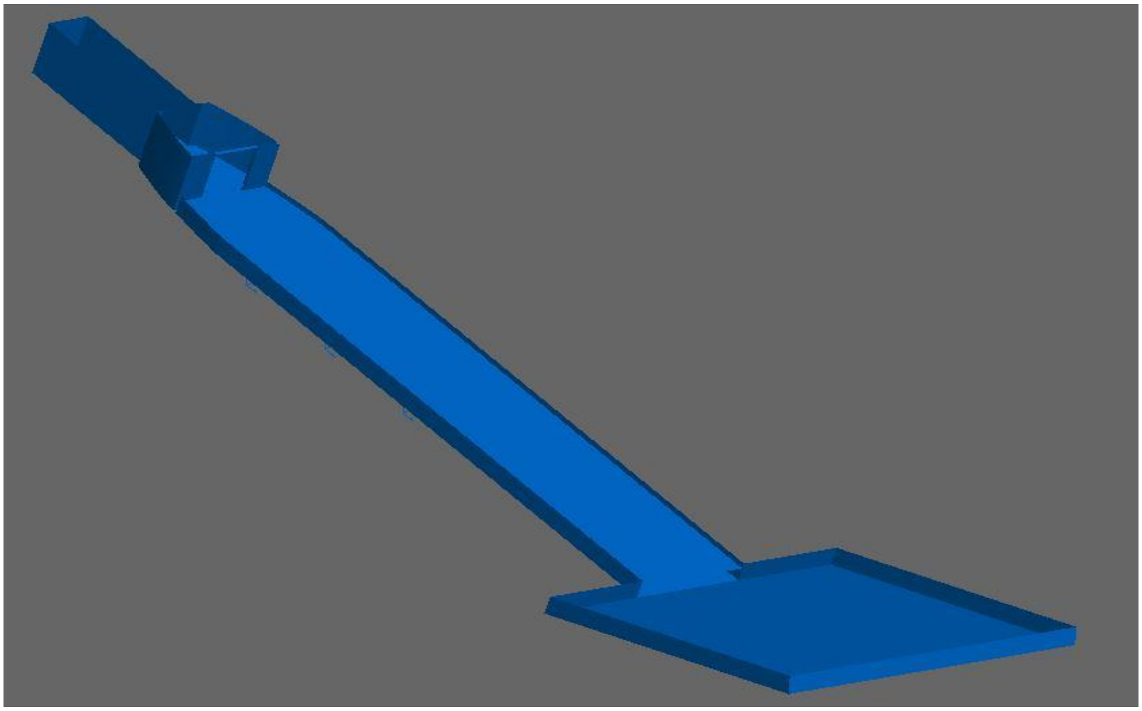

Figure 8. Location of the check dam in the flume

The graphs obtained from the simulations, shown in Figures 9 through 12, indicate that in the case without a check dam, the initial flow surge is recorded with high intensity at the first sensor (1.75 m) without encountering any physical barrier, then gradually diminishes in energy as it propagates downstream. The simultaneous presence of distinct peaks at all three sensors (blue, orange, yellow) reflects the free passage of the flow along the flume.

For the check dam with an opening of 0.75 times the flume width, the graphs demonstrate that the flow passes almost unaffected by the check dam, exhibiting behavior similar to the case without any structure. The surge appears at all sensors with high amplitude and closely timed intervals, indicating the limited effectiveness of the structure in impeding sediment transport.

In the check dam with an opening of 0.5 times the flume width, the flow passes through the opening at a more uniform rate. The first sensor records a moderately delayed peak with balanced amplitude. At the second and third sensors, the flow exhibits reduced fluctuations and greater stability, with peaks appearing at closely spaced times. This behavior pattern indicates that this opening size provides an optimal balance between controlled passage and effective reduction of flow intensity downstream.

Conversely, in the check dam with an opening of 0.25 times the flume width, the initial surge encounters the dam body and accumulates upstream. It then passes abruptly through the narrow opening under high localized pressure. As a result, the first sensor records an early peak with high amplitude and severe fluctuations. Further downstream, due to significant flow passage restrictions, the arrival time of the peaks at the second and third sensors is delayed, and the peaks there are of lower amplitude with increased instability. This condition reflects the gradual energy loss of the flow and the transfer of fluctuations downstream along the flume.

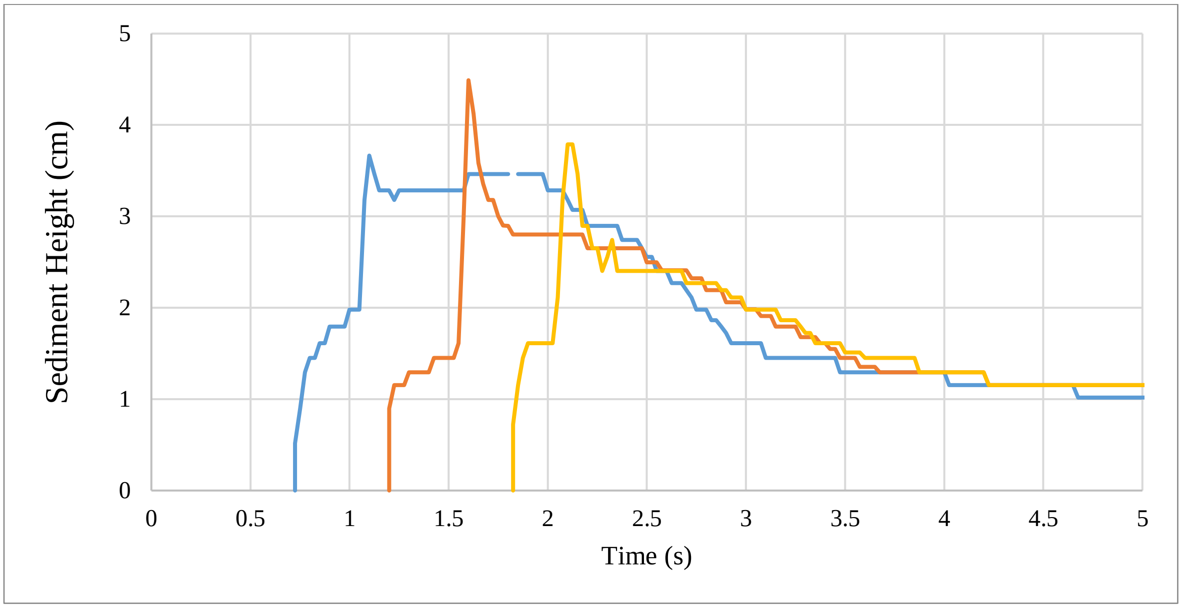

Figure 9. Time series of sediment height for the case without a check dam

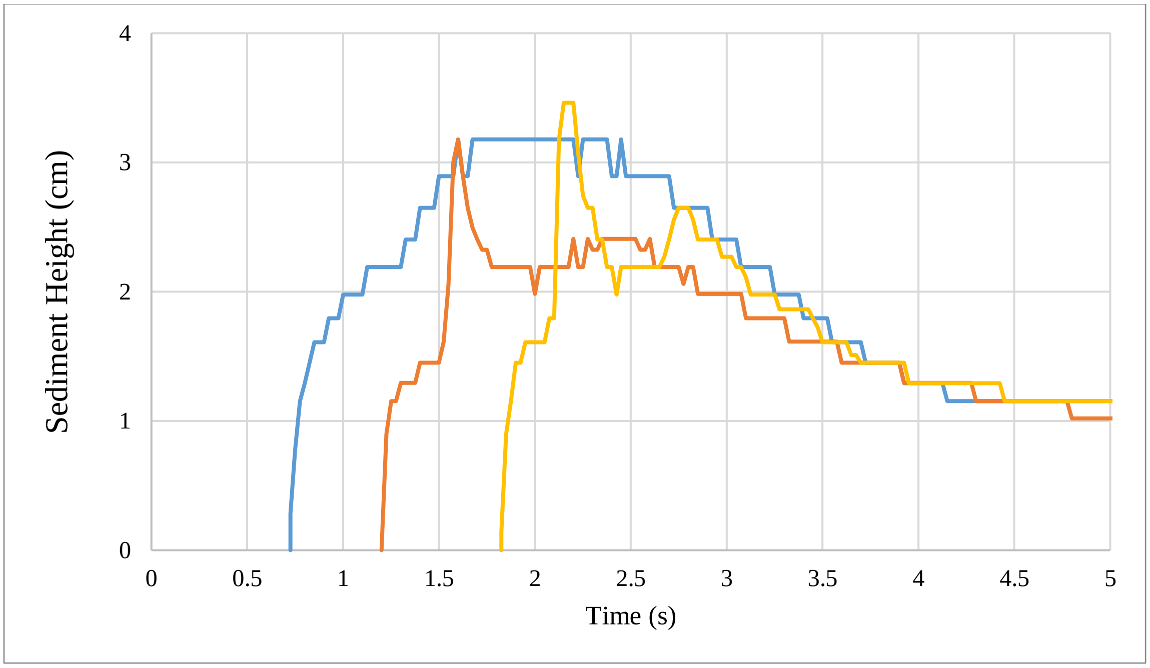

Figure 10. Time series of sediment height for the case with a check dam featuring an opening equal to 0.75 times the flume width.

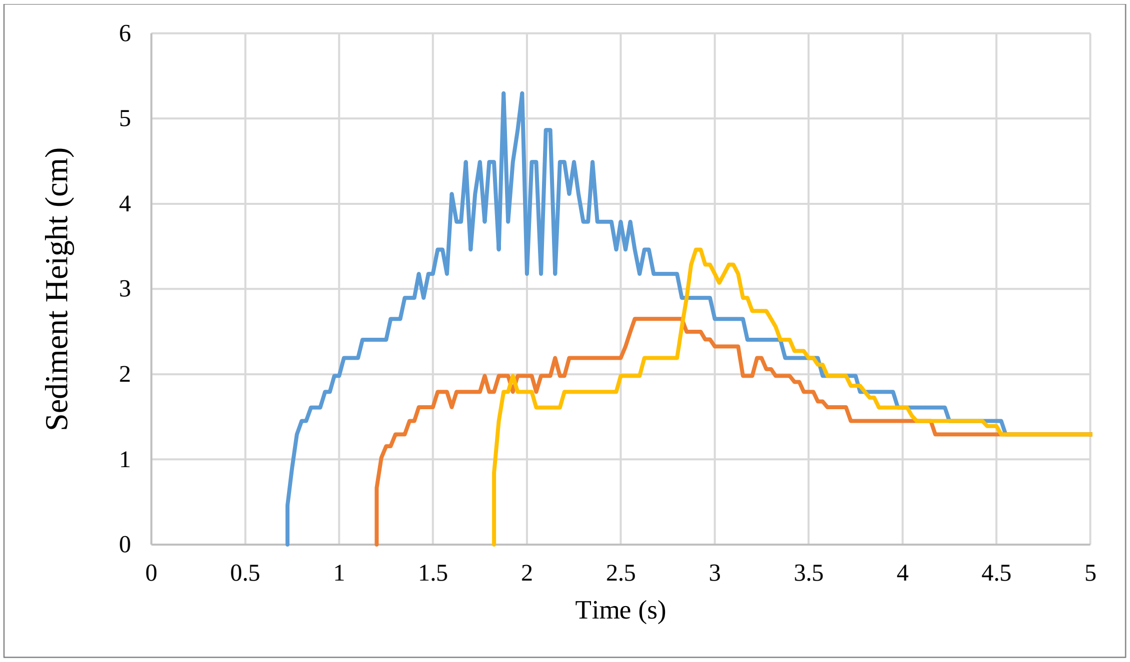

Figure 11. Time series of sediment height for the case with a check dam featuring an opening equal to 0.5 times the flume width.

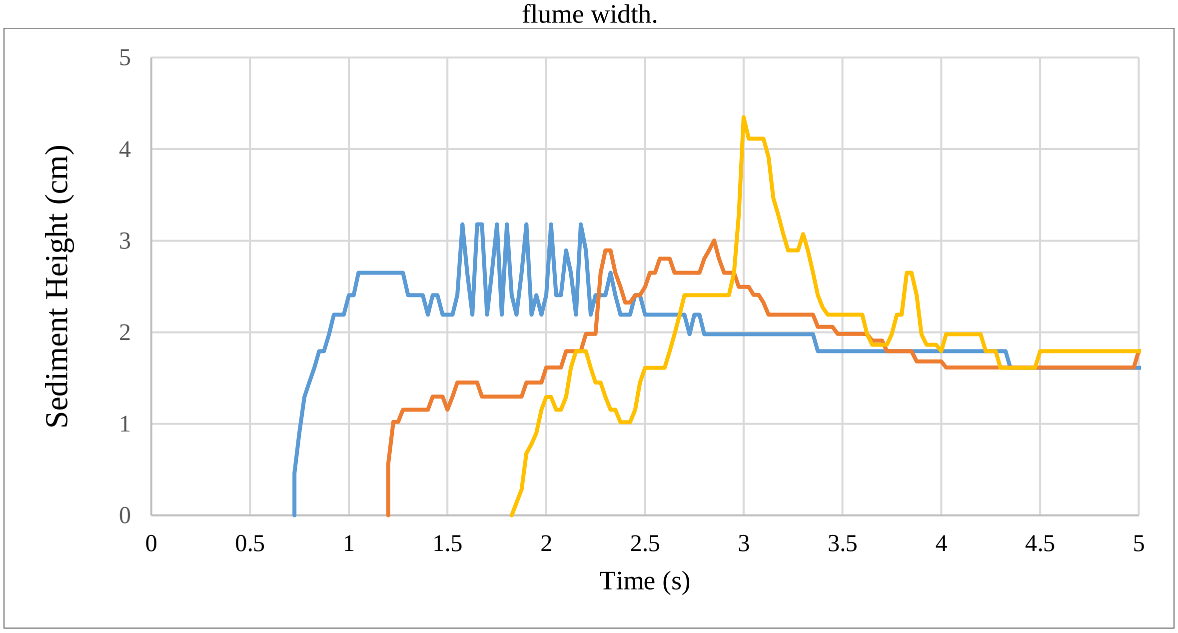

Figure 12. Time series of sediment height for the case with a check dam featuring an opening equal to 0.25 times the flume width.

In this section, the peak sediment elevation time at each sensor is analyzed. This analysis can provide a clearer understanding of the role that check dam openings play in controlling and directing debris flows. Before this, Figures 13 to 15 illustrate the time-dependent changes in sediment elevation for four different scenarios: the case without a check dam (red), and check dams with openings of 0.75 (yellow), 0.5 (blue), and 0.25 (green) times the flume width. These graphs correspond to measurements at the first, second, and third sensors, respectively. By analyzing these charts, the time of maximum sediment elevation (peak) at each sensor under the four tested conditions can be extracted, and these results are presented in Figures 16 to 18.

As seen in Figure 13, the amplitude of fluctuations recorded at Sensor 1, which is located closer to the check dam (approximately 0.87 meters from the inlet)—is significantly greater compared to Figures 14 and 15, which represent downstream sensors (Sensor 2 and 3), particularly in scenarios with openings of 0.25 and 0.5 times the flume width. This behavior can be attributed to the direct impact of the flow front striking the check dam and the resulting wave reflections. In these more constricted openings, part of the flow, after colliding with the check dam structure, encounters localized backflow and temporary accumulation of debris upstream of the dam. This leads to amplified oscillations in sediment elevation readings near the dam. In contrast, as the flow moves away from the point of initial impact (as seen at more distal sensors), it gradually transitions into a more stable and uniform condition, leading to reduced fluctuation amplitudes.

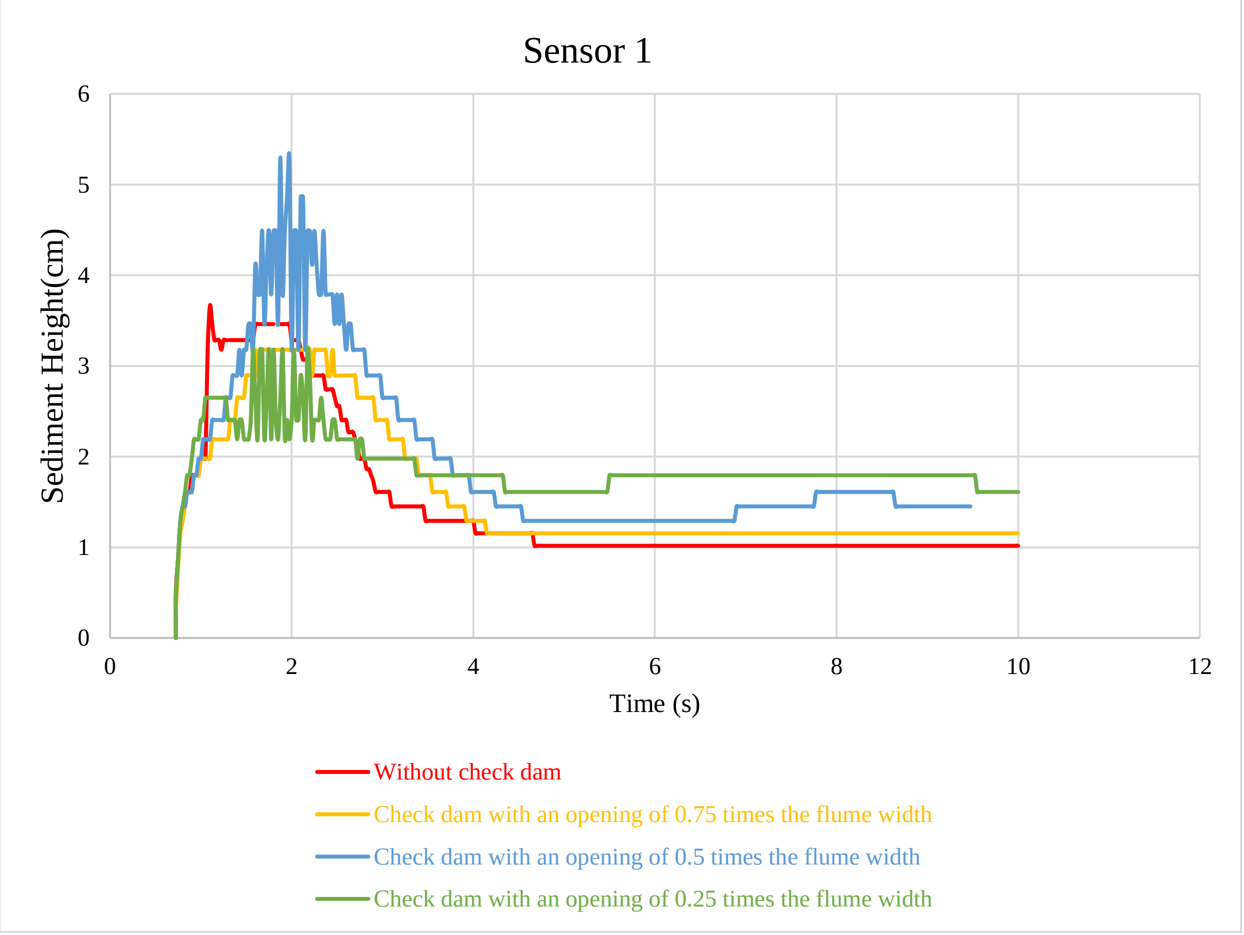

Figure 13. Time series of sediment elevation at Sensor 1 for the four simulated scenarios, illustrating differences in surge arrival, peak formation, and post-peak decay.

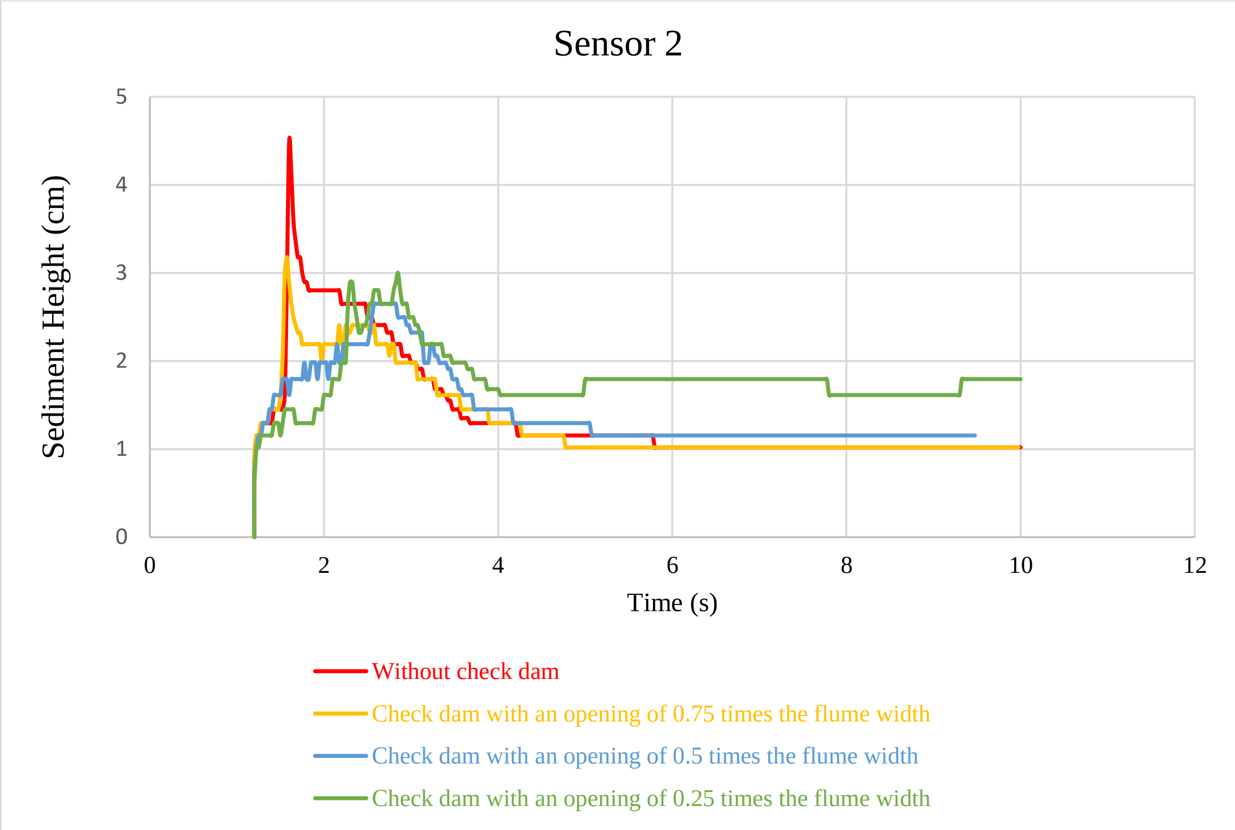

Figure 14. Time series of sediment elevation at Sensor 2 for the four simulated scenarios, illustrating differences in surge arrival, peak formation, and post-peak decay.

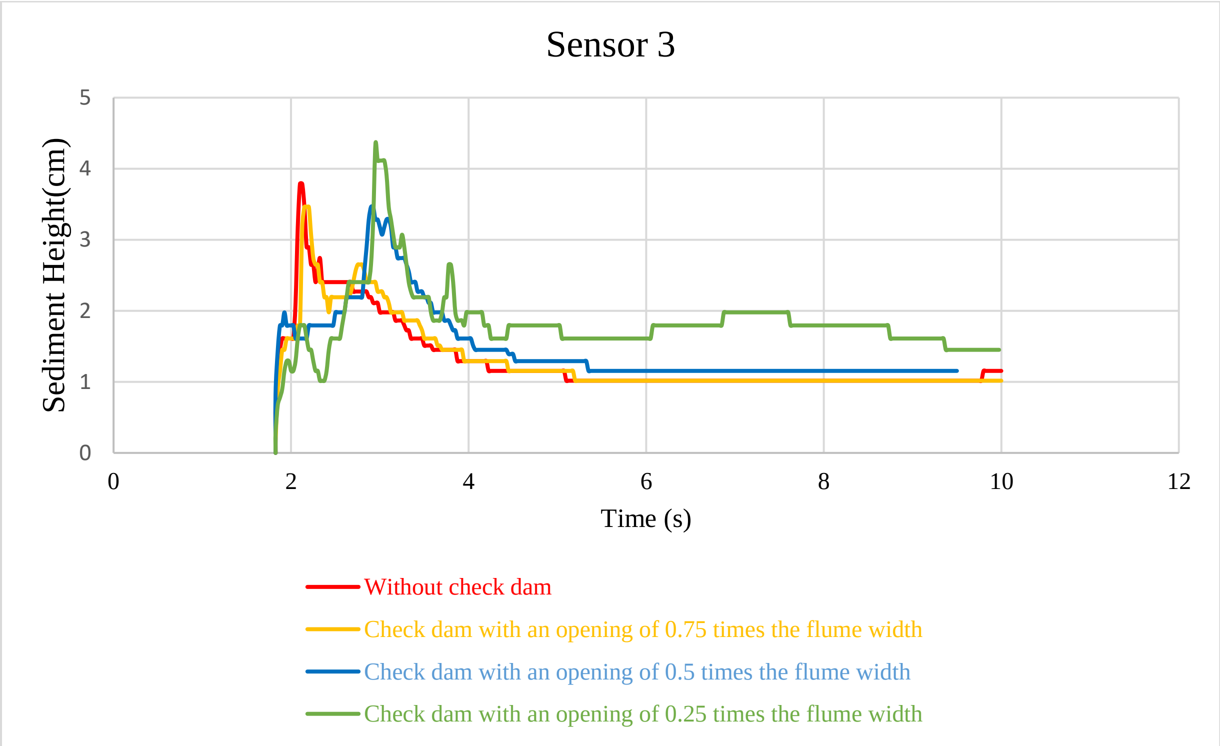

Figure 15. Time series of sediment elevation at Sensor 3 for the four simulated scenarios, illustrating differences in surge arrival, peak formation, and post-peak decay.

As shown in Figure 16, at Sensor 1, which is positioned closest to the check dam (approximately 0.87 meters from the flume inlet), a clear difference is observed in the time of peak sediment elevation among the three check dam scenarios compared to the no-dam case. The time differences for the peaks—relative to the no-dam condition—are recorded as 0.5, 0.87, and 0.47 seconds for opening widths of 0.75, 0.5, and 0.25 times the flume width, respectively. These values indicate that the presence and width of the check dam opening have a significant effect on the arrival time of the debris flow front and the occurrence of peak sedimentation near the structure.

Continuing with Figure 17, which corresponds to Sensor 2, it is observed that for the 0.75-width opening, there is no notable change in the timing of the peak compared to the no-dam scenario. However, for narrower openings, the time difference increases noticeably—0.97 seconds for the 0.5-width opening and 1.25 seconds for the 0.25-width opening. This delay reflects the role of narrower openings in decelerating the flow and extending the time required for the debris flow to reach downstream positions.

In addition, as shown in Figure 18, a similar pattern is observed at Sensor 3, which is located furthest downstream from the check dam. In this sensor, the time delay for the 0.75-width opening is negligible. However, for the narrower openings of 0.5 and 0.25 times the flume width, the time differences relative to the no-dam scenario are 0.8 and 0.9 seconds, respectively. This trend indicates that the influence of the check dam extends even to downstream locations, and reducing the opening width continues to affect the timing of sediment deposition throughout the flow path.

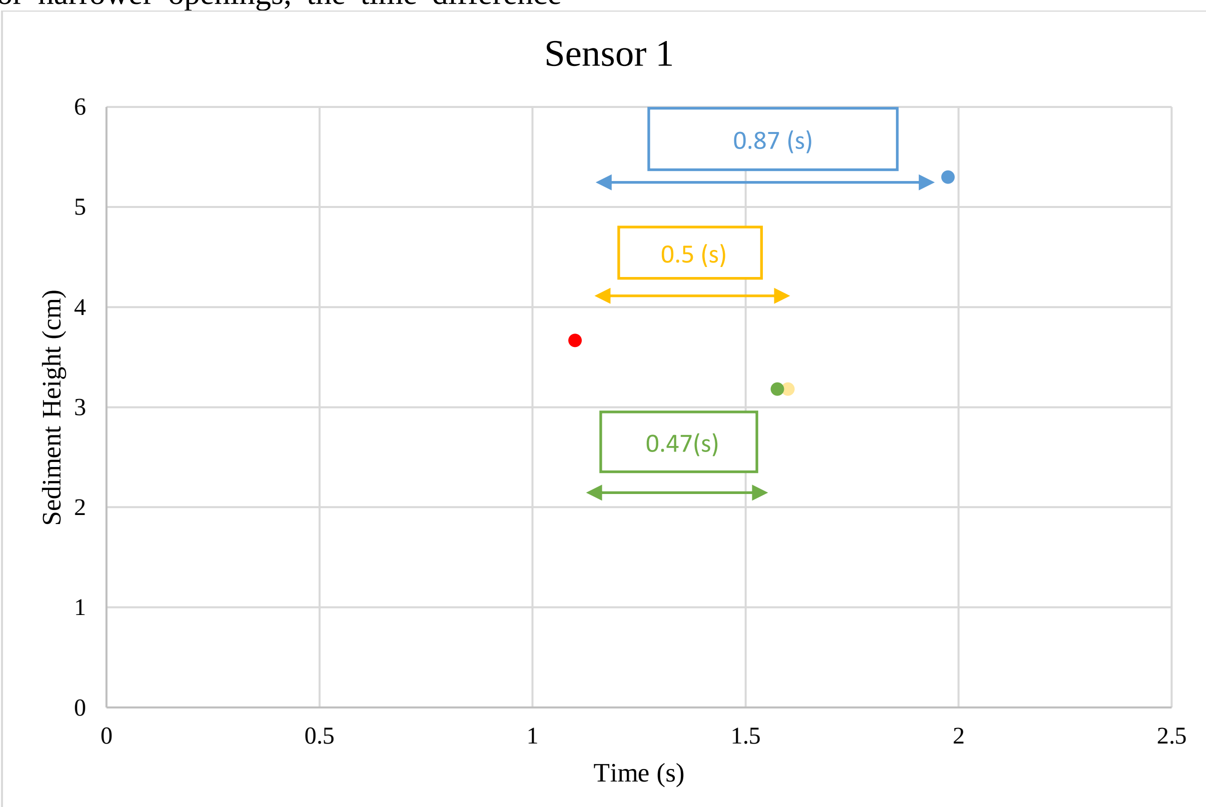

Figure 16. Timing of peak sediment elevation at Sensor 1 across the four simulated scenarios, highlighting differences in surge dynamics and peak delay.

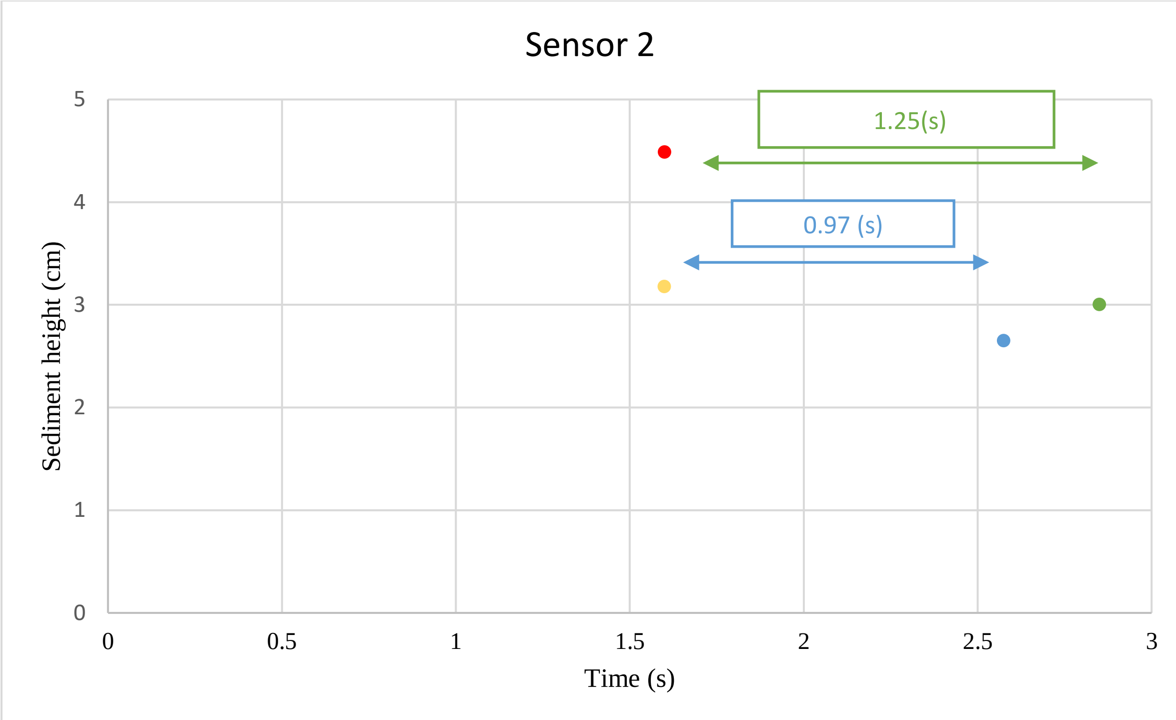

Figure 17. Timing of peak sediment elevation at Sensor 2 across the four simulated scenarios, highlighting differences in surge dynamics and peak delay.

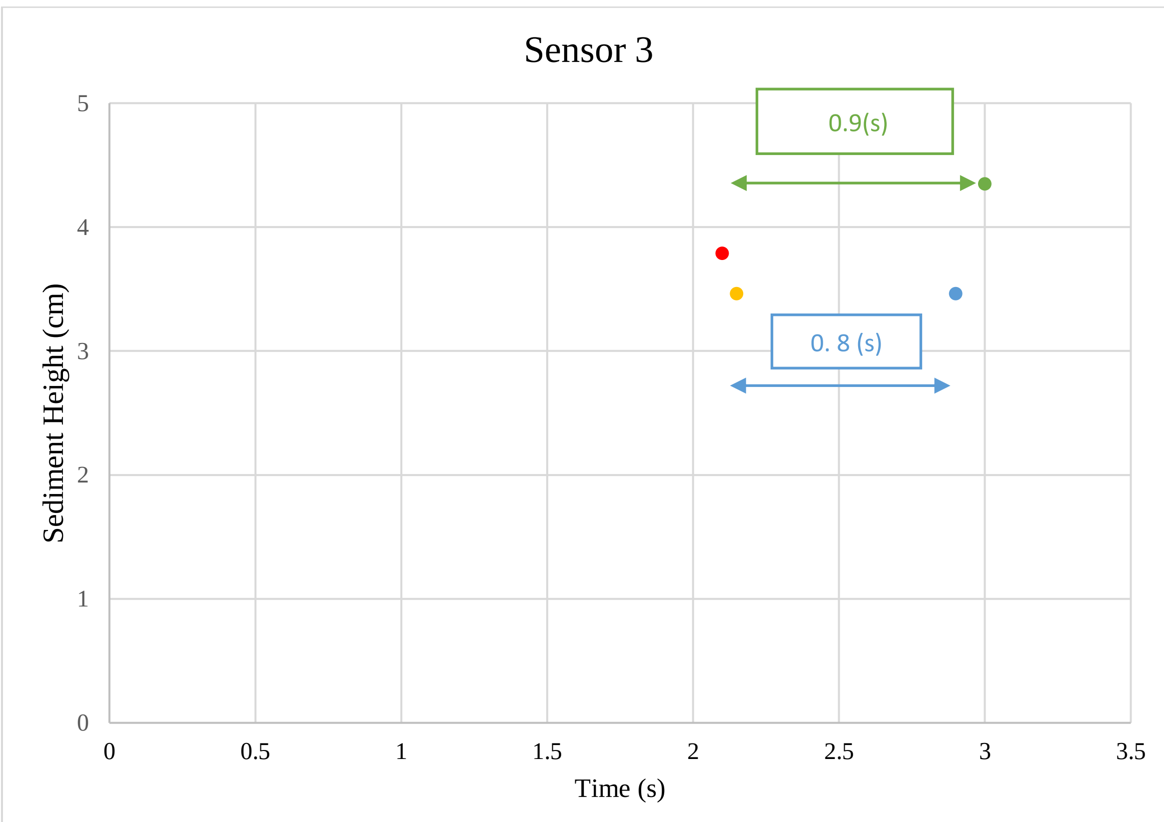

Figure 18. Timing of peak sediment elevation at Sensor 3 across the four simulated scenarios, highlighting differences in surge dynamics and peak delay.

In continuation of the analysis of Figures 16 through 18, the differences in the timing sequence of peak occurrence between the 0.25 and 0.5 channel-width openings at different sensor positions can be explained as follows:

At Sensor 1, which is located near the check dam and where the flow has not yet fully developed, the flow behavior is directly influenced by the initial impact with the check dam.

In the case of the 0.25-width opening, due to the narrowness of the gap, the flow rapidly accumulates in front of the check dam. As localized pressure increases (see Figure 19), a sudden and forceful passage through the opening occurs, resulting in an earlier peak being recorded at Sensor 1 (at 0.47 seconds).

In contrast, the 0.5-width opening, with its larger aperture, allows for a more gradual and widespread passage of flow, accompanied by lower localized pressure (see Figure 20), which leads to a delayed peak registration (at 0.87 seconds).

At Sensors 2 and 3, which are located farther downstream and where the flow has more room to develop, the behavior is primarily influenced by the overall discharge rate through the check dam.

With the 0.25-width opening, the severe restriction in flow passage causes the debris to move more slowly through the narrow gap (see Figure 21), resulting in a greater delay before reaching downstream areas. Consequently, the sediment height peak is recorded significantly later (e.g., 1.25 seconds at Sensor 2).

Conversely, with the 0.5-width opening, the flow passes through the gap more quickly (see Figure 22), allowing the debris flow to reach downstream sections sooner, such that the peak appears at an earlier time (0.97 seconds).

discussed. Based on Froude similarity, the hydrodynamic behavior (energy dissipation, peak delay, and sediment trapping efficiency) observed at laboratory scale can be qualitatively extended to prototype conditions, although grain-size distribution, rheological heterogeneity, and boundary roughness may influence quantitative responses. The validated model provides a physically consistent framework suitable for extrapolation to real-scale mountain torrents after adjusting inflow rheology and geometry. These clarifications define the model's applicability limits and potential for large-scale implementation.

In addition to the geometric effects examined in this study, the model's sensitivity to other governing parameters can be explored in future work. Important factors include: (1) sediment concentration and grain-size distribution, which strongly influence mixture rheology and interphase momentum exchange; (2) variations in bed slope, which modify the front velocity, energy dissipation, and deposition patterns; and (3) fluid properties and effective viscosity, which directly affect flow stability and surge formation. Although these parameters were not varied in the present study—because the focus was placed on the influence of opening size—their effects have been conceptually discussed here to provide a broader perspective and to guide future sensitivity-driven investigations.

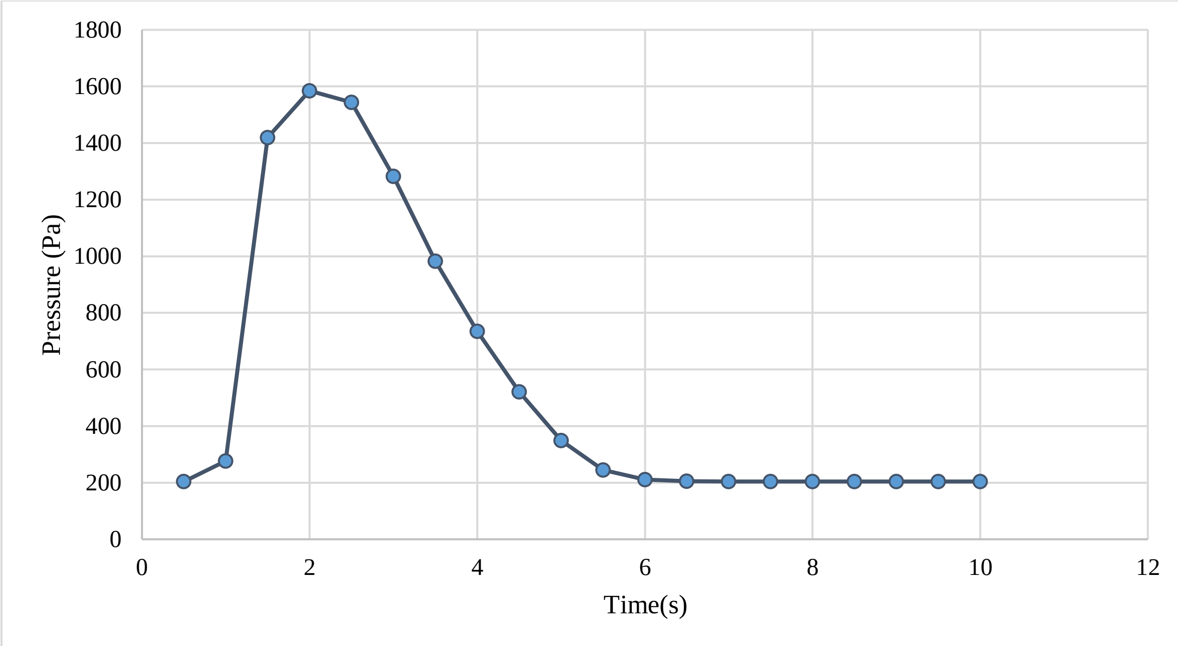

Figure 19. Pressure distribution around the check dam with an opening width equal to 0.25 times the channel width

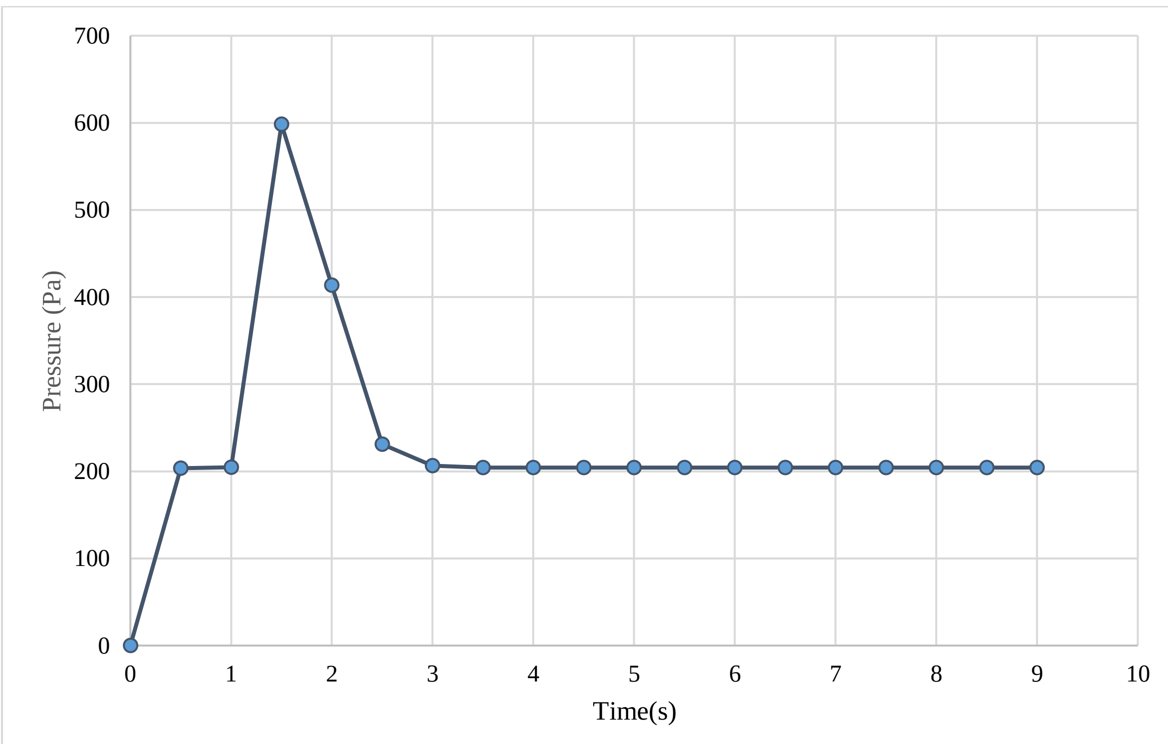

Figure 20. Pressure distribution around the check dam with an opening width equal to 0.5 times the channel width.

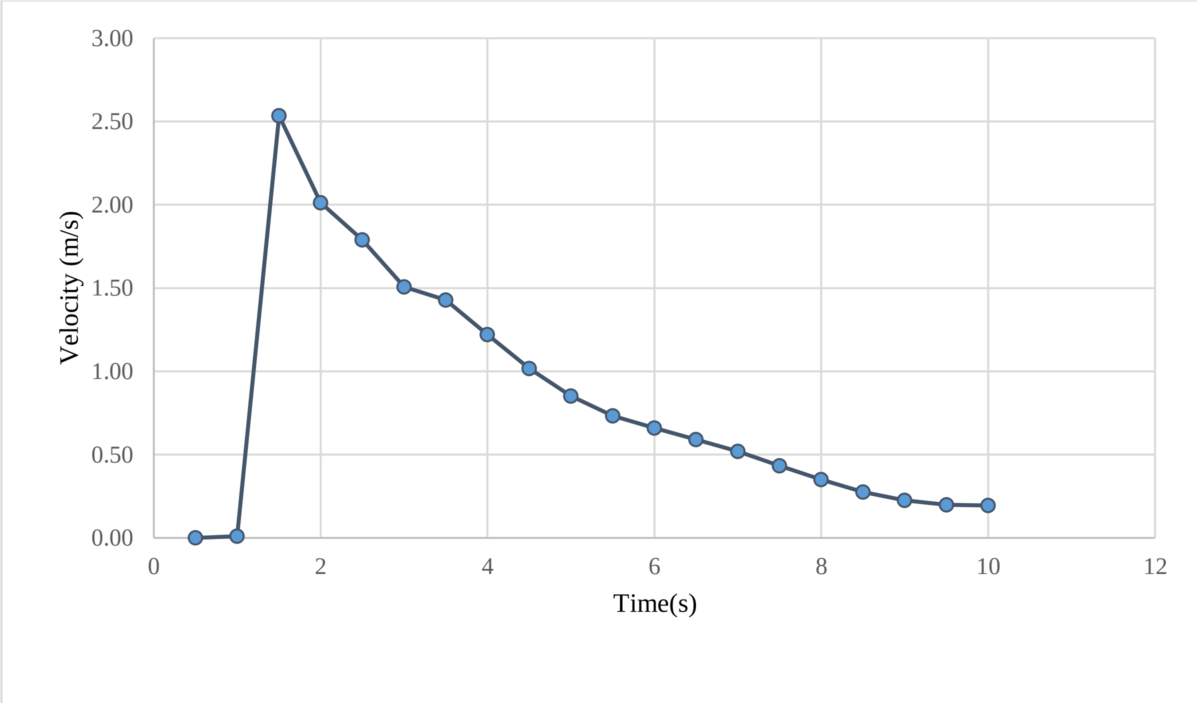

Figure 21. Velocity at Sensor 2 for the check dam with an opening width equal to 0.25 times the channel width.

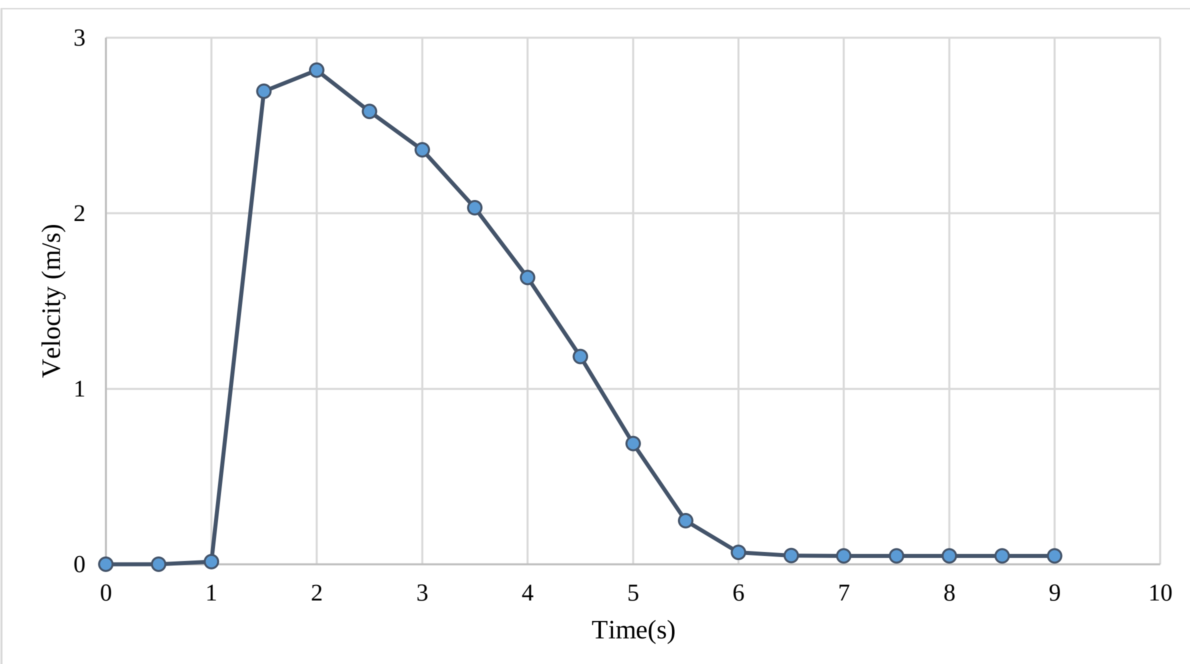

Figure 22. Velocity at Sensor 2 for the check dam with an opening width equal to 0.5 times the channel width.

3.3. Uncertainty and Error Assessment

Experimental uncertainties mainly originate from the limitations of the measurement devices used during the flume experiments. The ultrasonic sensors employed to record the free-surface elevation and debris-flow front position have a resolution of approximately ±0.5 mm, which introduces minor fluctuations in the detected surge arrival time and peak sediment height. Similarly, the bed-mounted pressure transducers exhibit a calibration tolerance of about ±2 Pa, leading to small deviations in the measured basal pressure. These sources of uncertainty were partially mitigated through repeated experimental trials and temporal filtering during data processing; however, they still represent a baseline uncertainty that must be considered when comparing numerical and experimental results.

Numerical uncertainties are primarily associated with spatial and temporal discretization as well as solver convergence behavior. A mesh-independence analysis using three grid sizes (0.9×10^6, 1.2×10^6, and 1.6×10^6 cells) showed that the variation in peak flow depth at Sensor S2 remained below 1.8%, confirming mesh-independent behavior for the selected resolution (~1.2 million cells). Temporal discretization errors were minimized by enforcing a Courant number below 0.3 throughout the simulation, ensuring numerical stability and preventing artificial oscillations in the computed flow depth and pressure fields. These measures collectively improve the reliability of the numerical framework.

Additionally, uncertainties related to the modeling framework and rheological parameters influence the predictive capability of the simulations. The multiphase Eulerian–Eulerian approach and the chosen rheological formulations for the slurry and debris phases depend on calibrated material parameters derived from laboratory characterization. Variations in sediment size distribution, water content, and solid concentration may introduce deviations in the predicted surge dynamics. Nonetheless, parameter selection was guided by experimental observations and established rheological correlations, ensuring that the model maintains physical consistency within realistic limits.

3.4. Model Limitations and Future Improvements

In this study, the slurry phase was modeled using a Herschel–Bulkley–type rheology (implemented through the HerschelBulkleyDebrisFlow model), which captures both the yield-stress characteristics and shear-thinning behavior of the mixture. The coarse-granular debris phase was represented using the Pudasaini- Coulomb-ViscoPlastic rheology, which accounts for friction-dominated and viscoplastic effects typical of gravel-rich debris flows. These rheological formulations provide a substantially more realistic representation of debris-flow behavior compared to simplified Newtonian assumptions.

Nevertheless, the adopted rheological models still involve certain simplifications to ensure computational feasibility in full 3D transient simulations. For example, both formulations rely on bulk-averaged material parameters derived from laboratory characterization, which do not explicitly resolve particle-scale interactions or grain-size variability. However, despite these necessary simplifications, the numerical predictions demonstrated strong agreement with experimental observations, indicating that the selected rheologies accurately reproduce the bulk hydrodynamics of the debris flow. This subsection therefore clarifies the applicability and limitations of the adopted material models and highlights potential directions for future refinement, such as incorporating polydisperse particle effects or DEM–CFD coupling.

4. Conclusion

4.1. Influence of Check Dams on Peak Timing and Flow Propagation

The presence of a check dam significantly affects both the timing of sediment peak occurrence and the flow development pattern along the flume. Compared to the no-dam scenario, narrower openings—particularly the one with 0.25 times the channel width—resulted in noticeable delays in peak detection at downstream sensors, indicating a loss of energy and more effective flow control.

4.2. Reduced Effectiveness with 0.75-Width Opening

The check dam with an opening equal to 0.75 times the flume width showed limited capability in obstructing sediment and flow passage. Its performance closely resembled that of the dam-free condition, with minimal differences in peak timing across sensors and high flow amplitudes. This pattern indicates uncontrolled, free-flowing conditions past the dam.

4.3. Balanced Behavior with 0.5-Width Opening

The 0.5-width opening demonstrated the most balanced performance, enabling controlled sediment transport while also ensuring effective trapping. The flow remained relatively stable, with moderate fluctuations and well-timed peak arrivals at all sensors. This behavior reflects effective flow attenuation and a more uniform downstream distribution—traits of a hydraulically stable system.

4.4. Aggressive Flow Dynamics with 0.25-Width Opening

In the case of the narrowest opening, 0.25 times the flume width, a strong local pressure buildup occurred upstream of the check dam. This led to a sudden, high-velocity burst of flow through the gap. As a result, the first sensor recorded an early, high-amplitude peak accompanied by intense fluctuations. While this configuration was more effective at trapping debris, it caused instability downstream.

Notably, the shape of the sediment-height curves at downstream sensors served as a practical indicator of hydraulic stability: smooth, gradually declining post-peak trends suggest stable flow, while jagged, oscillating curves point to turbulent, unstable behavior.

4.5. Increasing Delay in Peak Timing with Downstream Distance

As the distance from the dam increased, the influence of the opening width on peak timing became more pronounced. Interestingly, in the first sensor—closest to the dam—the 0.25-width opening produced an earlier peak than the 0.5-width opening due to the sudden release of pressurized flow.

4.6. Summary and Engineering Implications

Peak delay alone does not reliably indicate check-dam performance, as the narrowest opening (0.25W) produced long delays but also caused unstable, high-pressure surges and intense downstream fluctuations.

The 0.5-width opening provided the most favorable hydraulic behavior, enabling controlled debris passage with reduced fluctuations, more predictable timing, and lower energy loss.

Stable post-peak sediment-height curves reflect improved hydraulic stability, which reduces structural stress and erosion and enhances downstream safety and early-warning reliability.

4.7. Concluding remarks

Ultimately, check dam effectiveness must be evaluated through a comprehensive set of criteria, including flow rate moderation, amplitude of fluctuations, timing delays, and overall hydraulic stability. Based on this study, the dam with an opening equal to 0.5 times the flume width presents itself as the optimal solution. These findings provide practical insights for the engineering design of real-world check dams to manage debris flows in mountainous regions. In addition, the validated numerical model developed in this study can be extended to evaluate other types of debris-flow control structures, including slit dams with staggered openings, permeable embankments, and guiding channels. Such extensions would allow for the development of more generalized and comprehensive design guidelines for debris-flow mitigation in real-world applications.

Funding

No funding was received.

Conflicts of Interest

The authors declare that they have no conflicts of interest regarding the publication of this paper.

References

Albadawi, A., Donoghue, D. B., Robinson, A. J., Murray, D. B., & Delauré, Y. M. C. (2013). Influence of surface tension implementation in volume of fluid and coupled volume of fluid with level set methods for bubble growth and detachment. International Journal of Multiphase Flow, 53, 11-28. https://doi.org/10.1016/j.ijmultiphaseflow.2013.01.005

Baselt, I., Queiroz de Oliveira, G., Fischer, J. T., & Pudasaini, S. P. (2021a). Evolution of stony debris flows in laboratory experiments. Geomorphology, 372, 107431. https://doi.org/10.1016/j.geomorph.2020.107431

Berberović, E., Van Hinsberg, N. P., Jakirlić, S., Roisman, I. V., & Tropea, C. (2009). Drop impact onto a liquid layer of finite thickness: Dynamics of the cavity evolution. Physical Review E - Statistical, Nonlinear, and Soft Matter Physics, 79 (3), 036306. https://doi.org/10.1103/PhysRevE.79.036306

Bohorquez, P. (2012). Finite volume method for falling liquid films carrying monodisperse spheres in Newtonian regime. AIChE Journal, 58 (8), 2486-2498. https://doi.org/10.1002/aic.13863

Chen, S. C., & Wu, C. Y. (2014). Debris flow disaster prevention and mitigation of non-structural strategies in Taiwan. Journal of Mountain Science, 11 (2), 438-450. https://doi.org/10.1007/s11629-014-2987-3

Damián, S. M., & Nigro, N. M. (2014). An extended mixture model for the simultaneous treatment of small-scale and large-scale interfaces. International Journal for Numerical Methods in Fluids, 75 (8), 573-591. https://doi.org/10.1002/fld.3906

Huebl, J., & Fiebiger, G. (2005). Debris-flow mitigation measures. In Debris-flow Hazards and Related Phenomena (pp. 445-487). Springer Berlin Heidelberg. https://doi.org/10.1007/3-540-27129-5_18

Li, P., Zhang, X., & Lu, X. (2019). Three-dimensional Eulerian modeling of gas–liquid–solid flow with gas hydrate dissociation in a vertical pipe. Chemical Engineering Science, 196, 200-215. https://doi.org/10.1016/j.ces.2018.10.053

Matthias, J., & O. H. (2005). Debris-flow Hazards and Related Phenomena. Springer. https://doi.org/10.1007/b138657

Mizuyama, T. (2008). Structural countermeasures for debris flow disasters. International Journal of Erosion Control Engineering, 1 (2), 38-43. https://doi.org/10.13101/ijece.1.38

Shrestha, B. B., Nakagawa, H., Kawaike, K., & Baba, Y. (2008). Numerical and experimental study on debris-flow deposition and erosion upstream of a check dam. Proceedings of Hydraulic Engineering, 52, 139-144. https://doi.org/10.2208/prohe.52.139

Tanhapour, M., & Banihabib, M. E. (2019). Determination of the rainfall threshold for debris flow occurrence in a part of Alborz mountainous basins. Watershed Engineering and Management, 11 (3), 575-588. https://doi.org/10.22092/ijwmse.2018.115111.1346

Voight, B. (1990). The 1985 Nevado del Ruiz volcano catastrophe: Anatomy and retrospection. Journal of Volcanology and Geothermal Research, 42 (1-2), 151-188. https://doi.org/10.1016/0377-0273(90)90075-Q

Vu, T. (2019, December). Structural and non-structural strategies for debris flow disaster prevention and mitigation. ResearchGate. https://www.researchgate.net/publication/342917635_Structural_and_non-structural_strategies_for_debris_flow_disaster_prevention_and_mitigation

Zhang, Y., Lyu, L., & Li, P. (2022). An optimized volume of fluid method for modelling three-dimensional debris flows: Implementation in OpenFOAM, validation, and application in the Aiwa Watershed, Beijing. Computers and Geotechnics, 144, 104651. https://doi.org/10.1016/j.compgeo.2022.104651

Zhuang, J., Cui, P., Wang, G., Chen, X., Iqbal, J., & Guo, X. (2015). Rainfall thresholds for the occurrence of debris flows in the Jiangjia Gully, Yunnan Province, China. Engineering Geology, 195, 335-346. https://doi.org/10.1016/j.enggeo.2015.06.006